An intrinsically disordered region of Drosha selectively promotes miRNA biogenesis, independent of tissue-specific Microprocessor condensates

Bing Yang[1]; Brian Galletta[2]; Nasser Rusan[2] and Katherine McJunkin[1]

[1]National Institute of Diabetes and Digestive and Kidney Diseases Intramural Research Program, National Institutes of Health, 50 South Drive, Bethesda, MD 20815

[2]National Heart, Lung, and Blood Institute, National Institutes of Health, 10 Center Drive, Bethesda, MD 20815

Abstract

Precise control of miRNA biogenesis is of extreme importance, since mis-regulation of miRNAs underlies or exacerbates many disease states. The Microprocessor complex, composed of DROSHA and DGCR8, carries out the first cleavage step in canonical miRNA biogenesis. Despite recent advances in understanding the molecular mechanism of Microprocessor, the N-terminal region of DROSHA is less characterized due its high intrinsic disorder. Here we demonstrate that Microprocessor forms condensates with properties consistent with liquid-liquid phase separation (LLPS) in select tissues in *C. elegans*. While DRSH-1/Drosha recruitment to granules is only partially dependent on its intrinsically disordered regions (IDRs), one of these N-terminal IDRs is crucial for biogenesis of a subset of miRNAs and normal development. A cis region of an IDR-dependent miRNA confers IDR-dependence to another miRNA, suggesting that the IDR recognizes sequences or structures in the miRNA primary transcript. Future studies will further elucidate the specificity of this interaction and the putative role of Microprocessor condensates.

Introduction

microRNAs (miRNAs) are a class of small non-coding RNAs around 22-23 nucleotides in length (Bartel, 2018). Their biogenesis starts with transcription of primary miRNA transcripts (Cai et al., 2004; H. Kim et al., 2024; Lee et al., 2004) which are then recognized and cleaved by the Microprocessor complex composed of DROSHA and DGCR8 (also known as PASH-1 in *C. elegans*) resulting in precursor miRNAs with sizes from ~60 to 80nt (Denli et al., 2004; Gregory et al., 2004; Han et al., 2004, 2006; H. Kim et al., 2024; Landthaler et al., 2004; Lee et al., 2003; Zeng et al., 2005). The precursor miRNA is then exported from the nucleus to the cytoplasm by exportins (Bohnsack et al., 2004; Büssing et al., 2010; Lund et al., 2004; Yi et al., 2003; Zeng & Cullen, 2004). In the cytoplasm, endonuclease DICER recognizes and cleaves the precursor into a mature miRNA duplex (Bernstein et al., 2001; Grishok et al., 2001; Hutvágner et al., 2001; Ketting et al., 2001; Knight & Bass, 2001), which is then loaded into an Argonaute protein to form the miRNA induced silencing complex (miRISC) and target downstream mRNA molecules for gene silencing (Gregory et al., 2005; Grishok et al., 2001; Hammond et al., 2001; Mourelatos et al., 2002; Tabara et al., 1999).

Primary miRNA (pri-miRNA) recognition and cleavage is orchestrated by the Microprocessor complex (Denli et al., 2004; Gregory et al., 2004; Han et al., 2004, 2006; H. Kim et al., 2024; Landthaler et al., 2004; Lee et al., 2003; Zeng et al., 2005). Structural and *in vitro* biochemical studies have intensively characterized the interaction interfaces between the Microprocessor complex and the pri-miRNA molecule; this work has revealed several sequence elements that define substrate optimality of pri-miRNAs, such as the UG motif near the basal junction (Auyeung et al., 2013; Fang & Bartel, 2015; Garg et al., 2024; Jin et al., 2020; B. Kim et al., 2017; Kwon et al., 2016; Li et al., 2020; T. A. Nguyen et al., 2015; Partin et al., 2020). However, most of these studies were carried out using truncated DROSHA without the N-terminus due to aberrant aggregation of the full-length protein (T. A. Nguyen et al., 2015). Therefore, in contrast to the

intensive characterization of the enzymatic domains, the function of the N-terminus of DROSHA is poorly understood. The N-terminal region of DROSHA is the least conserved region of the protein (B. Kim et al., 2017). In vertebrates, the N-terminus is highly enriched in prolines, arginines, and serines, and enriched in overall disorderedness (Son et al., 2023). Global miRNA deficiency was observed upon endogenous deletion of the DROSHA N-terminus (A.A. 1-396) through CRISPR in cell lines (Prabhakar et al., 2023). Another recent report identified a major proteolytic DROSHA isoform that lacks the N-terminal proline-rich disordered domain (PRD – A.A. 1~198) and described the function of the PRD in mediating pri-miRNA processing of a subset of miRNAs encoded in introns (Son et al., 2023).

Over the last decade, liquid-liquid phase separation (LLPS) has been linked to numerous biological phenomena, and LLPS is thought to be the driving force behind the formation of a diverse array of membrane-less organelles, such as stress granules, P-bodies, paraspeckles, and P granules (Banani et al., 2017; Brangwynne et al., 2009). Scaffold molecules initiate the formation of the scaffold matrix through multivalent interactions and then recruit client molecules to further mature these condensates (Banani et al., 2016). Intrinsically disordered regions (IDR) of proteins are hypothesized to be one of the main providers of multivalency (Mitrea & Kriwacki, 2016). Liquid-like biomolecular condensates have been proposed to support diverse functions such as compartmentalization and concentration of biochemical reactions or storage of macromolecules (Putnam et al., 2023). A key question in the field is how frequently observable biomolecular phase-separated droplets represent "incidental condensates" that do not add functionality beyond that provided by the soluble population of proteins outside of the condensates (Putnam et al., 2023).

In this study, we describe nuclear condensate formation of the Microprocessor complex in select *C. elegans* tissues. FRAP experiments suggest that the Microprocessor foci are dynamic, consistent with formation through LLPS. Based on co-localization analysis, we conclude that these DRSH-1 condensates are distinct from known nuclear granules. We then investigate the function of the predicted IDRs in regulating DRSH-1 condensate formation and miRNA biogenesis. We observe that an IDR is required for the biogenesis of a subset of miRNAs and for normal development. However, the roles of the Drosha IDR in miRNA biogenesis and animal development appear to be independent of the condensate formation.

Results

Drosha forms distinct nuclear condensates in *C. elegans*

To assess the distribution of DRSH-1 in *C. elegans*, we fused GFP to the DRSH-1 C-terminus by knocking it in at the endogenous locus using CRISPR/Cas9 (Figure 1A). The wild type viability and fertility exhibited by *drsh-1::gfp* animals suggested that this fusion protein is fully functional (Figure S1A). As expected, we observed DRSH-1::GFP localization primarily in the nucleus across different tissues (Figure 1B). In most tissues, the nuclear DRSH-1::GFP signal was diffuse (e.g. germ line in Figure 1B). Interestingly, we found prominent granule-like distribution of DRSH-1 in

nuclei of early embryos and nuclei of both larval and adult hypodermis cells (Figure 1C). The diameter of these granules ranges from those at the diffraction limit (≤250nm) up to ~1µm (Figure S1B). The proportion of DRSH-1::GFP that was localized to the granules was ~2% of the total nuclear signal in the hypodermal cells (Figure S1C). To rule out that GFP contributes to granule formation, we also tagged DRSH-1 with highly monomeric mScarlet (Bindels et al., 2017) and consistently saw granule-like distribution in early embryo and larval and adult hypodermal nuclei (Figure S1D). To determine whether the DRSH-1 granules contain both components of the Microprocessor, we generated a double tagged *drsh-1::gfp; pash-1::mscarlet* strain and observed strong co-localization of DRSH-1::GFP and PASH-1::mScarlet in these granules (Figure 1D). Thus, the Microprocessor complex clusters in bright granule-like foci in specific tissues.

Given the granule-like distribution pattern, we wondered whether these granules are LLPS-mediated biomolecular condensates. To test this hypothesis, we performed fluorescence recovery after photobleaching (FRAP) experiments to bleach an entire focus and monitor fluorescence recovery by the influx of DRSH-1::GFP from the surrounding nucleoplasm. DRSH-1::GFP foci recovered quickly after bleaching ($t_{1/2}$ = 4s ± 0.9s, SEM, n=23) with the intensity recovered to around 50% of the pre-bleaching level, indicating that the condensates consist of both a mobile fraction that exchanges with the nucleoplasmic fraction rapidly and also an immobile DRSH-1::GFP fraction that exchanges very slowly or not at all (Figure 1F-G).

To determine if DRSH-1 granules coincide with known nuclear granules, we imaged fluorescently-tagged DRSH-1 alongside markers of nuclear granules: paraspeckles marked by NONO-1::GFP, nuclear stress granules labeled by HSF-1::GFP, RNA polymerase II transcriptional condensates marked by AMA-1::GFP, FUS granules labeled by FUST-1::GFP, splicing bodies marked by FOX-1::GFP, and heterochromatic foci marked by MET-2::mKate (Hills-Muckey et al., 2022; Pham et al., 2021). Although a previous report suggested that DGCR8 localizes to paraspeckles (Jiang et al., 2017), we failed to observe co-localization between DRSH-1 and NONO-1 foci (Figure 1H and S1F). Furthermore, we did not observe any co-localization between DRSH-1 and other known nuclear granule markers (Figure 1H and S1E-F), with the exception of methyltransferase MET-2, where colocalization was only rarely observed: 17% (10 out of 59) of DRSH-1 granules colocalized with MET-2 (Figure S1G). In conclusion, we have found that the Microprocessor complex forms distinct nuclear foci in selected tissues in *C. elegans* possibly through LLPS.

DRSH-1 is a client protein in granule formation

Because we observed DRSH-1 granules that are distinct from known nuclear granules, we interrogated whether DRSH-1 itself is the driver of the putative LLPS or rather a client of a condensate formed by another scaffold molecule. If DRSH-1 is the driver of its own phase separation, then all DRSH-1 above the protein's characteristic saturation concentration (c_{sat}) would phase separate and the nucleoplasmic level would be at or below c_{sat}. This would predict that tissues with observable DRSH-1::GFP foci have higher overall nuclear concentration of DRSH-

1::GFP than tissues lacking DRSH-1::GFP foci. When we quantified the mean DRSH-1::GFP intensity in nuclei of hypodermis cells and adjacent germ cells (which lack DRSH-1::GFP foci), no significant difference of the average intensities was observed (Figure S1H-I). This observation suggests that granule formation is not solely due to DRSH-1::GFP protein concentration, and DRSH-1 is an LLPS client protein in hypodermal nuclei. However, because only ~2% of DRSH-1::GFP resides in foci in hypodermal nuclei (Figure S1C), very small differences in concentration (as little as 2% higher in hypodermal nuclei) could underlie tissue specificity of granule formation; our detection method may not be sensitive enough to distinguish such small differences.

To further test whether granule formation depends on DRSH-1 concentration, we genetically controlled the concentration of DRSH-1. To this end, we engineered a situation in which the *drsh-1::gfp* allele is heterozygous with a *drsh-1* null allele (hemizygous), thus resulting in lower concentration of DRSH-1::GFP (Figure 2A). We then characterized the hemizygous strain in comparison to its homozygous *drsh-1::gfp* parental strain. In the hemizygous strain, we observed that the overall hypodermal nuclear signal of DRSH-1 was reduced to about 60% of the control (Figure 2B-C). If DRSH-1::GFP granule formation in the wild type setting is driven by DRSH-1::GFP exceeding its c_{sat} by ~2%, then DRSH-1::GFP granules would be abolished in the hemizygous setting which reduces DRSH-1::GFP concentration well below the theoretical c_{sat}. Instead, granules were still formed, though their intensity was reduced to a similar extent as the overall nuclear signal (Figure 2C-D). Reduced granule intensity in the hemizygous background held true when quantifying all foci together (Figure S2A) or when comparing the first or second brightest focus in each nucleus (Figure 2D, Figure S2A). (Intensity was the most accurate measurement of granule formation; we were unable to accurately measure granule size due the diffraction limit, and we were unable to precisely count granule number as many granules were not much brighter than the nucleoplasm, preventing accurate image thresholding.) Overall, DRSH-1::GFP does not obey a simple c_{sat} predictive model, and thus it likely is a client of other molecules in its recruitment to granules in specific tissues.

Deletion of DRSH-1 IDRs reduces but does not abolish granule recruitment of DRSH-1

The N-terminal region of DROSHA contains intrinsically disordered regions and is proline-enriched (Son et al., 2023). Although the proline-enriched nature is not conserved in *C. elegans* DRSH-1, the disorderedness is conserved (Son et al., 2023). Numerous reports have established the significant contribution of IDRs to LLPS (Dignon et al., 2020); therefore we wondered whether the IDRs of DRSH-1 are important for mediating the recruitment of Microprocessor to granules. To understand the function of the N-terminus of DRSH-1 in its distribution and functionality, we utilized IUPred to predict disorderedness of the region and identified two putative disordered domains (Erdős & Dosztányi, 2020; Mészáros et al., 2018), namely IDR1 and IDR2 (Figure 3A). We used CRISPR to establish mutants in which IDR1, IDR2, or both IDRs are deleted, in both wild type and *drsh-1::gfp* backgrounds. Using the different IDR deletions in the *drsh-1::gfp* background, we assayed the expression of these truncated proteins through western blotting.

171 Migration of the truncated proteins was consistent with their expected sizes. The mutations did not
172 have significant effects on DRSH-1::GFP protein level in the whole animal samples (Figure 3B).
173
174 To understand the impact of the IDR deletions on the granule recruitment of DRSH-1::GFP, we
175 imaged the hypodermal nuclei of each of the mutants and compared them to wild type. Overall
176 nuclear signal was slightly reduced in ΔIDR1, slightly increased in ΔIDR2, and similar to wild
177 type in the ΔIDR1/2 background (Figure 3D). (Although these results partially agree with trends
178 observed by western blot, differences are likely due to the difference in sample type: whole animal
179 samples with mixed tissues for western blot versus hypodermal tissue nuclei for imaging.) We
180 found that ΔIDR1 results in slightly lower intensities of granules than wild type; this was the case
181 either when quantifying all foci together (Figure S3A) or when comparing the first or second
182 brightest focus in each nucleus (Figure 3E, S3B). If the IDR1 has a direct role in DRSH-1
183 recruitment to granules, then its effect on granule intensity should be greater than that of the
184 hemizygous genotype, which had a similar impact as ΔIDR1 on overall nuclear signal (reducing it
185 to 60% of wild type). However, the reduction in granule intensity was comparable to that in the
186 hemizygous background (Figure 3E, Figure 2D), suggesting that the IDR1 itself has no impact on
187 granule recruitment beyond its effect on DRSH-1::GFP concentration. The ΔIDR2 mutation alone
188 did not significantly affect the intensity of all foci quantified together (Figure S2A) and had
189 inconsistent impacts on the intensity of the two brightest granules per nucleus (Figure 3E, Figure
190 S3B). Finally, the ΔIDR1/2 combined mutation reduced granule intensity without affecting overall
191 nuclear DRSH-1::GFP signal (Figure 3D-E, Figure S3). Because the combined mutation – but not
192 the single IDR deletions – decouples granule intensity from DRSH-1::GFP level (reducing
193 intensity without affecting level), this suggests that the two IDRs may act redundantly to promote
194 granule recruitment. This reduction in granule intensity is again mild, indicating that the IDRs are
195 not strictly required for granule recruitment of DRSH-1::GFP, and other parts of the protein also
196 likely contribute. Overall, the IDR mutations had moderate impacts on granule formation, which
197 in the case of ΔIDR1 reflected its impacts on DRSH-1::GFP level.
198
199 **An IDR is important for biogenesis of a subset of miRNAs in *C. elegans***
200 Despite the modest impact of individual IDR mutations on DRSH-1 level and granule recruitment,
201 we observed a strong impact on development in ΔIDR1 mutant animals. The ΔIDR1 but not
202 ΔIDR2 animals showed bursting (vulval rupture) with 9% penetrance, while ΔIDR2 animals were
203 superficially wild type (Figure 4A and 4B). Similar results were obtained when the deletions were
204 introduced in wild type or *drsh-1::gfp* backgrounds, confirming not only the phenotype but also
205 the functionality of the *gfp* tagged DRSH-1 protein (Figure 4B). The ΔIDR1/2 double mutant
206 mirrored the ΔIDR1 phenotype with 9% penetrance of bursting, indicating that IDR1 and IDR2 do
207 not act redundantly with respect to this aspect of development (Figure 4B).
208
209 The vulval bursting phenotype we observed is reminiscent of loss-of-function mutations in the
210 miRNA pathway (Grishok et al., 2001; Reinhart et al., 2000). To examine the impact of the IDRs

211 on miRNA biogenesis, we performed small RNA sequencing of the ΔIDR1 and ΔIDR2 mutants at
212 the fourth larval (L4) and adult stages. Sequencing analysis using either total piRNAs or spike-ins
213 as a normalization method showed very similar differential expression results (Figure 4 and S4).
214 Among a total of ~200 miRNAs detected by sequencing (DEseq2 normalized mean reads > 5), 49
215 miRNAs were significantly downregulated in ΔIDR1 in comparison to wild type (DEseq2 $\log_2$FC
216 < -1, $p_{adj} < 0.05$) at the L4 stage, and only two miRNAs were upregulated ($\log_2$FC > 1, $p_{adj} < 0.05$)
217 (Figure 4C). Moreover, we observed a very similar pattern of expression changes in ΔIDR1
218 animals compared to wild type at the adult stage, with 41 miRNAs downregulated and two
219 upregulated (Figure 4D). Changes in miRNA levels caused by ΔIDR1 were highly correlated
220 between the two stages (Figure 4E), with 80% of the downregulated miRNAs in common between
221 L4 and adult (Fisher's exact test $p < 1x10^{-17}$). Thus the ΔIDR1 mutation causes a consistent
222 selective defect in miRNA production affecting the same set of miRNAs across life stages. Unlike
223 ΔIDR1 mutants, only minor changes in miRNA profile were observed in the ΔIDR2 mutants, with
224 modest amplitude of changes and poor consistency between life stages (Figure 4F-H). In
225 conclusion, IDR1 deletion results in a strong, selective defect in miRNA production across
226 different life stages, whereas IDR2 deletion has little impact.
227
228 Next, we sought to determine whether the miRNA abundance changes we observed in ΔIDR1
229 animals are due to Microprocessor defects rather than other indirect effects. We first validated the
230 downregulation that was observed in deep sequencing for six mature miRNAs by qPCR (Figure
231 4I). We also included two miRNAs (*mir-1*, *mir-80*) as controls that were not differentially
232 expressed in the sequencing data, nor were they altered in ΔIDR1 mutants by qPCR (Figure 4I). If
233 the prominent downregulation of select miRNAs observed in ΔIDR1 animals is due to a defect in
234 Microprocessor activity, then decreased mature miRNA levels should be accompanied by
235 increased pri-miRNA levels. We measured pri-miRNA levels by qPCR and observed that this is
236 the case: in all examined cases in which the mature miRNA decreased in ΔIDR1, the corresponding
237 pri-miRNA level increased (Figure 4I). Furthermore, the examined mature miRNAs that were not
238 sensitive to ΔIDR1 (*mir-1, mir-80*) also showed no changes in pri-miRNA level (Figure 4I).
239 Overall, this suggests that DRSH-1 IDR1 is crucial for the efficient Microprocessing of a select
240 subset of miRNAs.
241
242 Importantly, neither the bursting phenotype nor the molecular phenotype were due to IDR1's effect
243 on DRSH-1 level or granule recruitment, since neither phenotype was observed in the DRSH-
244 1::GFP hemizygous setting which displayed similar reduction in DRSH-1::GFP levels and granule
245 recruitment as in ΔIDR1 (Figure 2). Small RNA sequencing revealed that the 60% dosage of
246 DRSH-1::GFP and resulting lower granule intensity in the DRSH-1::GFP hemizygous setting did
247 not result in significant changes in miRNA expression profile (Figure S2B). Moreover, the
248 hemizygous worms were superficially wild type without any noticeable phenotypes (no bursting).
249 Therefore, the effects of the ΔIDR1 mutation are not recapitulated by orthogonal means of

reducing protein dosage and granule recruitment, demonstrating instead that the IDR1 plays a specific role in Microprocessor-mediated cleavage of select substrates.

Microprocessor-independent miRNA expression rescues DRSH-1 IDR1 mutation phenotype

The bursting phenotype of ΔIDR1 strongly resembles loss of function phenotypes of the *let-7* family of miRNAs (Reinhart et al., 2000; Slack et al., 2000). Thus, we reasoned that the bursting may be due to decreased expression of *let-7* or its paralogs (Abbott et al., 2005). Indeed, among the miRNAs that were significantly downregulated in the ΔIDR1 mutant are two *let-7* paralogs (dubbed *let-7* sisters), *mir-84* and *mir-241* (Figure 4C-D). To test whether the downregulation of these two miRNAs is responsible for the bursting phenotype, we utilized a mirtron-based expression system that allows for mature miRNA biogenesis that bypasses the Microprocessor step (Dexheimer et al., 2020). Briefly, a miRNA precursor is embedded as a small intron in a GFP mini-gene, and pre-mRNA splicing followed by debranching of the intron lariat (rather than Microprocessor-mediated cleavage) thus liberates the precursor miRNA for further maturation (Figure 5A). We generated transgenes that expressed both *mir-84* and *mir-241* from such mirtron cassettes, wherein transcription was driven by the miRNAs' endogenous promoters. Two independent extrachromosomal array transgenes were made, and both showed good rescue of mature *mir-84* and *mir-241* expression to near wild type levels by qPCR (Figure 5B). We then assessed their impact on the phenotype of the ΔIDR1 mutant. Both of the *mir-84 mir-241* mirtron-based rescuing transgenes strongly rescued the vulval bursting phenotype of the ΔIDR1 mutant to 0-1% bursting (Figure 5C), while a control transgene lacking the mirtrons provided no rescue (9% bursting). Thus, DRSH-1 IDR1 is required for normal viability because of its role in promoting biogenesis of select miRNAs, especially that of the *let-7* sisters *mir-84* and *mir-241.*

***Cis* sequences of primary *mir-241* confer sensitivity to IDR1 deletion**

We observed that ΔIDR1 mutation in DRSH-1 induces a consistent defect in Microprocessing affecting a subset of pri-miRNA substrates; we therefore sought to understand what underlies the specificity of dependence upon the IDR1 for biogenesis. To this end, we tested the association between various features of pri-miRNAs and their sensitivity to the IDR1 deletion (Figure 6A). Although multiple sequence motifs associated with optimal Microprocessor primary miRNA substrates are well annotated in mammalian cells (Auyeung et al., 2013; Fang & Bartel, 2015; Jin et al., 2020; Kwon et al., 2016, 2019; T. A. Nguyen et al., 2015; Partin et al., 2017), most of these motifs are not enriched in *C. elegans* pri-miRNAs, with the exception of the midBMW and mGHG motifs (Kwon et al., 2019; Li et al., 2020, 2021), neither of which predicted dependency on IDR1 (Figure S5A-B). A recent effort to characterize the *C. elegans* Microprocessor *in vitro* has advanced our understanding of its cleavage parameters and identified a DROSHA dsRNA recognition sites (DRES) motif that correlates with substrate optimality (T. L. Nguyen, Nguyen, Ngo, & Nguyen, 2023; T. L. Nguyen, Nguyen, Ngo, Le, et al., 2023). We examined whether the *in*

289 *vitro* Microprocessor cleavage score or the DRES score were correlated with miRNA sensitivity
290 to ΔIDR1 and again found no association (Figure 6B and 6C).
291
292 We then analyzed the features of primary miRNA secondary structure predicted by miRGeneDB
293 (Clarke et al., 2025), including apical loop length, stem length, mismatch count, lower stem length,
294 and bulges. However, no significant correlation was observed between any of these structural
295 features and ΔIDR1 sensitivity (Figure 6D and S5C-D). Additionally, we considered the genomic
296 contexts of pri-miRNAs, including clustering status and intronic/exonic position that were
297 previously reported to be important for the processing of certain subsets of miRNAs (Donayo et
298 al., 2019; Fang & Bartel, 2020; Hutter et al., 2020; Janas et al., 2011; Lataniotis et al., 2017;
299 Pawlicki & Steitz, 2008; Shang et al., 2020; Slezak-Prochazka et al., 2013; Thivierge et al., 2024;
300 Truscott et al., 2016). Moreover, the N-terminus proline-enriched domain of human DROSHA has
301 been shown to mediate intronic miRNA biogenesis (Son et al., 2023). However, our analysis did
302 not show any significant difference in ΔIDR1 sensitivity between these miRNA categories (Figure
303 5E).
304
305 At the organismal level, miRNA expression is known to be spatially regulated and often exhibit
306 tissue and cell-type specificity (Aboobaker et al., 2005; Alberti et al., 2018; Brosnan et al., 2021;
307 Landgraf et al., 2007; Martinez et al., 2008). Given that we observed tissue-specific formation of
308 granules and obvious developmental phenotypes related to hypodermal cells, we wondered
309 whether tissue of expression could contribute to ΔIDR1 sensitivity. To test this hypothesis, we
310 replaced the upstream sequence of an ΔIDR1-insensitive miRNA (*mir-80*) with the upstream
311 sequences of an ΔIDR1-sensitive miRNA (*mir-241*). Intriguingly, we noticed that this ~2kb
312 fragment conferred ΔIDR1 sensitivity to *mir-80* (Figure 6F, mut1). To determine whether this
313 fragment conferred sensitivity by driving *mir-80* expression in the hypodermis, we then replaced
314 the sequence upstream of *mir-80* with a known hypodermis promoter (*dpy-7*), but this did not
315 confer sensitivity to ΔIDR1 to *mir-80,* unlike the 2kb *mir-241* upstream fragment (Figure 6F, mut2).
316 We thus revisited the 2kb sequence and divided it into the 1.7kb fragment upstream of the pri-*mir-*
317 *241* TSS (R. A.-J. Chen et al., 2013; Gu et al., 2012; Kruesi et al., 2013; Saito et al., 2013) and the
318 remaining 293bp that lies between the TSS and the predicted basal junction of pri-*mir-241*. We
319 then replaced the corresponding fragments in the *mir-80* locus with the fragments of the *mir-241*
320 locus. Strikingly, the 293bp cis element, but not the 1.7kb upstream fragment conferred sensitivity
321 of *mir-80* to ΔIDR1 (Figure 6F, mut4 and mut3), similar to the full 2kb fragment of *mir-241*. This
322 suggests that flanking sequences near the base of the pri-miRNA hairpin determine dependence on
323 DRSH-1 IDR1 for maximally efficient processing.
324
325 **Discussion**
326 In this study, we describe the formation of distinct nuclear DRSH-1 foci in select tissues in *C.*
327 *elegans*, consistent with recruitment to LLPS condensates. Although a previous report hinted at
328 the potential co-localization between DGCR8 and paraspeckles (Jiang et al., 2017), our study

329 provides the first evidence of Microprocessor condensates in living cells. We demonstrate that
330 DRSH-1 is a client protein in condensate formation since the simple phase separation model
331 defined by $>c_{sat}$ of DRSH-1 is incompatible with the behavior of these granules. What scaffolds
332 Microprocessor foci and governs their tissue specificity will be a crucial question as more
333 components of these granules are identified. The current study is also limited by the diffraction
334 limit (~250nm) of our imaging methods; further characterization of the granules by super
335 resolution microscopy will provide finer details of the condensates' structure and potentially
336 identify smaller-scale clusters in tissues other than embryos and hypodermal cells. Which regions
337 of DRSH-1 itself are required for its recruitment to granules is another open question; the N-
338 terminal IDRs redundantly promote DRSH-1 granule recruitment, but their impact is modest,
339 suggesting other regions of the protein also support recruitment.
340
341 The ability of Microprocessor to be recruited to condensates may provide a new layer of
342 Microprocessor regulation that was not previously explored. A lack of conditions in which granule
343 formation is completely abolished limits our ability to assess their function. One possibility is that
344 the Microprocessor condensates are "incidental condensates" resulting from the biophysical
345 properties of the complex and the nuclear context but not providing functionality beyond that of
346 diffuse Microprocessor (Putnam et al., 2023). Understanding the factors involved in scaffolding of
347 Microprocessor-containing granules will aid in perturbing these foci to probe their function.
348
349 Whereas the DRSH-1 IDRs had a modest role in Microprocessor recruitment to granules and
350 modest effects on DRSH-1 concentration, IDR1 clearly contributes to Microprocessor function.
351 The ΔIDR1 mutants exhibited strong molecular and developmental phenotypes related to
352 Microprocessing defects. The vulval bursting phenotype observed in ΔIDR1 is clearly attributable
353 to loss of biogenesis of *let-7* miRNA family members, because this phenotype is rescuable by
354 Microprocessor-independent expression of *let-7* paralogs.
355
356 We have shown that DRSH-1 IDR1 strongly contributes to biogenesis of a subset of miRNAs,
357 independent of known features of *C. elegans* Microprocessor substrate optimality. A 5' flanking
358 region of an IDR1-sensitive miRNA conferred sensitivity to an IDR1-insensitive miRNA; this
359 interesting observation suggests that the cis-acting element in this region of the pri-miRNA could
360 be interacting with the IDR1 domain. The fact that miRNAs derived from the same primary
361 transcript behaved differentially in response to IDR1 deletion – i.e. *mir-54* is significantly IDR1-
362 sensitive, whereas both *mir-55* and *mir-56* did not respond to IDR1 deletion (Figure S6) – further
363 supports the model that a cis element very close to the miRNA hairpin could mediate IDR1-
364 dependence. These findings are interestingly similar to the involvement of cis elements in
365 determining pri-miRNA reliance on the N-terminal IDRs of human DROSHA, suggesting that
366 these sequence-divergent regions of orthologous proteins may maintain conserved function (Son
367 et al., 2023). Further studies should reveal what properties define the sequence or structural feature

368 that is recognized by the IDR domain and whether the recognition is direct or indirect through
369 other RNA binding proteins.
370
371 **Materials and Methods**
372 ***C. elegans* culture**
373 *C. elegans* were cultured using standard protocols at 20°C (Stiernagle, 2006). L4 and adult worm
374 samples were collected 48 h and 60 h after L1 synchronization, respectively.
375
376 **Genome editing**
377 Unless otherwise mentioned, strains generated in this study were engineered endogenously using
378 CRISPR-Cas9. CRISPR-Cas9 mediated genome editing is performed as previously reported (Yang
379 et al., 2020). In brief, IDT alt-R guide RNAs were annealed by mixing crRNA and tracrRNA to a
380 final concentration of 10µM each using IDT duplex buffer, which was then incubated at 95°C for
381 5 min followed by gradual temperature decline to room temperature. Repair templates provided
382 for CRISPR were column purified after PCR synthesis. Final injection mix contains annealed
383 gRNA at final concentration of 1µM, IDT Cas9 at final concentration of 2µM and repair template
384 at final concentration ~200-400ng/µl (Paix et al., 2014). A gRNA targeting *dpy-10* was used as a
385 co-CRISPR marker for selection (Arribere et al., 2014). After injection, Dpy animals were cloned
386 and singled as F1s. F2 animals were then genotyped for desired edits.
387 GFP donor fragments were amplified using plasmid pCM1.35 as a template and primers containing
388 ~35-55 bp homology arms (Merritt et al., 2008; Paix et al., 2014). mScarlet donor molecules were
389 amplified using plasmid pGLOW30 as a template and primers containing ~35-55 bp homology
390 arms (Witten et al., 2023). Promoter sequences of *mir-241*, *mir-84* and *dpy-7* were amplified from
391 wild type genomic DNA using primers listed in table S2. Transcription start sites were determined
392 using the Wormbase TSS database (R. A.-J. Chen et al., 2013; Gu et al., 2012; Kruesi et al., 2013;
393 Saito et al., 2013).
394
395 **Western Blotting**
396 Three 10cm NGM plates seeded with 2,000 L1s were cultured at 20°C for 60 h, until animals
397 reached adulthood. Animals were then rinsed off the NGM plates with M9 buffer and washed three
398 times with M9 before being pelleted and snap frozen. Upon thawing, the worm pellets were mixed
399 with equal volume of cold 2x worm lysis buffer (60 mM HEPES pH 7.4, 100 mM KCl, 0.4%
400 Triton X-100, 4 mM MgCl2, 20% glycerol, 4 mM DTT, 2× cOmplete, Mini, EDTA-free Protease
401 Inhibitor Cocktail) and lysed using a Bioruptor Pico (Diagenode) for 10 cycles (30 seconds on and
402 30 seconds off). Crude worm lysate was then cleared by centrifugation at 16,000x*g* for 10 min.
403 Protein concentration of the resulting supernatant was then quantified using BCA assay. Equal
404 amounts of protein were loaded onto a 4-15% gradient Tris Glycine gel (Biorad). Membranes were
405 then probed with anti-GFP antibody (Roche) at 1:1,000 and anti-tubulin antibody DM1A (Abcam)
406 at 1:1,000.
407

408 **Microscopy**
409 Fluorescent microscopy was performed using a Nikon Eclipse Ti2 microscope (Nikon Instruments,
410 Melville, NY, USA) equipped with a W1 spinning disk confocal head (Yokogawa, Life Science,
411 Tokyo, Japan), 405-, 488-, 561-, and 641-nm laser lines, a 100x/1.49 total internal reflection
412 fluorescence oil immersion objective (Nikon Instruments) and a Prime BSI cMOS camera
413 (Teledyne Photometrics, Tuscon, AZ, USA). Fluorescence recovery after photobleaching (FRAP)
414 was performed using an Opti-MicroScan unit with a 405 nm laser. Nikon Elements software was
415 used to control the microscope and to collect images (Nikon Instruments). Image analysis was
416 performed using FIJI (Image J; National Institutes of Health, Bethesda, MD, USA).
417
418 **FRAP**
419 FRAP experiments were performed using the microscope described above. Hypodermal cells
420 nearest the coverslip were selected for imaging in which a single confocal plane was acquired
421 using 2x2 binning. One prominent fluorescent focus was selected for FRAP using a 10 millisecond,
422 405 nm laser exposure, which was sufficient to partially photobleach the focus. Movies of a single
423 focal plane using the 488nm laser were then collected using 2x2 binning and one image/second.
424 Only movies where the partially photobleached focus stayed within the imaging plane were used
425 for analysis.
426
427 For analysis, total integrated fluorescence measurements of a region of interest including the
428 bleached focus were recorded at each timepoint. Background subtraction was performed using a
429 nuclear region of identical area adjacent to the focus. Correction for photobleaching resulting from
430 timelapse image acquisition using the 488nm laser was performed by using the decrease in
431 fluorescence across the entire image. Data was normalized by setting the average focus intensity
432 from 10 pre-bleach frames to 1, and the first post-bleach frame to 0. The frame containing the
433 bleaching laser pulse was excluded from the analysis. Figure 1F presents the average of all
434 recovery curves ± standard deviation with time 0 equal to 10 frames prior to bleaching. The $t_{1/2}$ of
435 recovery and immobile fraction from individual recovery curves were determined following fitting
436 (one phase association) using Prism (GraphPad, Boston, MA, USA).
437
438 **Fluorescence intensity measurements in hypodermal nuclei**
439 Confocal Z-stack images of hypodermal cells close to the coverslip in live worms were acquired
440 using the microscope described above. Only nuclei where the animal and the foci did not move
441 substantially during acquisition were selected for analysis. For measurements of DRSH-1::GFP
442 foci, the integrated fluorescence intensity of a region of interest around prominent foci from a
443 single imaging plane was measured using Image J. An adjacent region within the nucleus that lacks
444 DRSH-1::GFP foci was used for background subtraction. To determine the upper limit of focus
445 intensity per nucleus, the first and second brightest foci from each nucleus were identified and
446 quantified. The dimmest foci in the nucleus occasionally yielded negative values after
447 measurement because their intensity was so close to the noise floor. These foci were excluded from

448 the “All foci” analysis. As a result, “All foci” represents all foci that could be identified and
449 measured. Fluorescence intensity was normalized to the average intensity of the comparable
450 (“brightest or “all”) foci in nuclei from wild type DRSH-1::GFP worms during each imaging
451 session.
452
453 Measurements of the intensity of GFP in the whole nucleus and estimates of percent DRSH-1::GFP
454 residing in foci both utilized the same images as measurements of foci. However, due to movement
455 of the animals during Z-stack acquisition, only a subset of images could be used for these analyses.
456 Sum projections of the Z-slices containing the nucleus were generated, and the fluorescence
457 intensity of a region of interest containing the nucleus was measured. An adjacent region outside
458 of the nucleus, but within the same cell was used for background subtraction. Fluorescence
459 intensity was normalized to the average intensity of the nuclear GFP signal from wild type DRSH-
460 1::GFP worms for each imaging session. To determine the percentage of DRSH-1::GFP nuclear
461 signal that was in the foci, sum projections were made of each focus in a nucleus, and the
462 fluorescence intensity of a region of interest containing each focus in the resulting images were
463 measured. The sum of all the foci in each nucleus was then calculated and the divided by the total
464 nuclear fluorescence determined above.
465
466 **Brood size assay and bursting phenotype scoring**
467 Brood size assay was performed as previously described (Kotagama et al., 2024). In brief, L4
468 animals of each genotype were singled onto individual plates and transferred to fresh plates every
469 24 h until embryos were no longer produced. Bursting phenotype was assessed within 48 h after
470 animals reached L3 stage.
471
472 **Mirtron extrachromosomal array generation and maintenance**
473 Mirtron plasmids expressing *mir-241* (plasmid pBY139) and *mir-84* (plasmid pBY140) are cloned
474 into the pUC19 vector based on the previously described strategy (Dexheimer et al., 2020). In brief,
475 *mir-241* and *mir-84* promoter fragments are amplified from genomic DNA and assembled
476 upstream of a partial GFP coding sequence, with mirtron-encoding sequences inserted between
477 exons. Extrachromosomal arrays were generated by injecting a mix of mirtron plasmids (80 ng/µl
478 final concentration for each plasmid) and a *unc-119* rescuing marker pCFJ150 (50 ng/µl) (Frøkjaer-
479 Jensen et al., 2008) into *unc-119(-); drsh-1(ΔIDR1)* animals. Non-Unc transformants were selected
480 and maintained by picking non-Unc progeny.
481
482 **RNA extraction**
483 Bulk samples of L4 and adult stage animals were pelleted from 10cm NMG plates using M9 and
484 snap-frozen in 500µl TRIzol (Life Technologies) until use. Adult animals for Figures 4 and 5 were
485 handpicked in the quantity of one hundred per sample into 20 µl M9 buffer in Eppendorf tubes,
486 and 500µl TRIzol was added to each tube before snap freezing. Upon thawing, samples were
487 vortexed at room temperature for 15 min. 85 µl chloroform was added to each sample and mixed

488 thoroughly. Samples were then centrifuged at 16,000×*g* for 10 min at 4°C. The supernatant was
489 transferred to a fresh tube and an equal volume of 25:24:1 phenol:chloroform:isoamyl alcohol
490 pH=4.5 was added to the sample. Samples were then centrifuged at 16,000×*g* for 15 min at 4°C.
491 The upper aqueous phase was transferred to a fresh tube and an equal volume of isopropanol and
492 1 µl of GlycoBlue (Thermo Fisher Scientific) was added to the aqueous phase and mixed gently.
493 Samples were frozen at −80°C for 30 min and thawed on ice. RNA precipitation was carried out
494 at 20,000×*g* for 30 min at 4°C. The RNA pellets were then washed twice with 70% ethanol with 5
495 min of centrifugation at 4°C. Approximately 20 µl of RNase-free water was added to resuspend
496 the RNA.
497
498 **qPCR**
499 For miRNA qPCR, reverse transcription reactions were performed using miRNA-specific RT
500 primers with the Taqman microRNA Reverse Transcription (RT) Kit (Thermo Fisher Scientific).
501 For all samples, 1.66 µl of total RNA at 5 ng/µl was used in 5 µl RT reactions. RT reactions were
502 then diluted 1:4 and 1.33 µl was used in a 5 µl qPCR reactions using Taqman miRNA probes and
503 the Taqman Universal Mastermix II with UNG (Thermo Fisher Scientific). Reactions were run in
504 three technical replicates on the Applied Biosystems QuantStudio 6.
505
506 Primary miRNA qPCR was performed using KAPA SYBR Fast One-Step qRT-PCR Kit on
507 QuantStudio 6 Flex Real-Time PCR System using primers listed in Table S2. In brief, 1.33 µl of
508 total RNA 5 ng/µl was used in a 5ul qPCR reaction. Reactions were run in three technical replicates
509 for each sample.
510
511 **Small RNA sequencing and mapping**
512 Small RNA library preparation was adapted from the NEBNext small RNA library prep kit (New
513 England Biolabs) (Vieux et al., 2021). Briefly, spike-ins were added to 600 ng of total RNA prior
514 to library construction for each sample. Size selection was performed after reverse transcription
515 using 8% urea gel to purify 65-75 nt products. PCR was performed with 15 cycles followed by
516 purification using NEB Monarch PCR purification kit to remove primer dimers. Sequence analysis
517 was performed on the NIH high performance computing cluster. Adapter sequences were trimmed
518 using fastp (0.24.0) command fastp -L (S. Chen, 2023). The reference genome was customized by
519 combining *C. elegans* genome WS280 with an artificial chromosome containing the synthetic
520 spike-in sequences (Donnelly et al., 2022). Mapping was performed using Bowtie2 using the
521 following settings: --end-to-end --sensitive -q -U (Langmead & Salzberg, 2012). BAM files were
522 sorted and indexed using samtools 1.13 (Danecek et al., 2021). Reads were assigned to miRNAs
523 and piRNAs using htseq 0.13.5 (Putri et al., 2022) with the following settings: --mode union --
524 nonunique fraction -a 0. The htseq analysis on miRNAs was performed using a gff file modified
525 from mirGeneDB (Fromm et al., 2015). The htseq analysis on piRNAs was performed using a gff
526 file from https://www.pirnadb.org/ (Piuco & Galante, 2021). miRNA differential gene expression

was analyzed using DESeq2 analysis with default settings (Love et al., 2014) using total piRNA reads or spike-in reads for normalization.

Data availability

All primary sequence data have been deposited at NCBI Gene Expression Omnibus under accession number GSE289120. Reviewers may access the data using the following token: abqnacikpdgltyd.

Competing Interest Statement

The authors have not competing interests to declare.

Acknowledgements

We thank members of the laboratory and Baltimore Worm Club for helpful discussions. We thank Geraldine Seydoux for critical feedback on the manuscript. Multiple strains were obtained from the CGC, which is funded by NIH Office of Research Infrastructure Programs (P40 OD010440). WormBase was used for the design and execution of the study (Sternberg et al., 2024). This research was funded by the NIDDK Intramural Research Program (ZIADK075147) and NHLBI Intramural Research Program (ZIAHL006126).

Author Contributions

B.Y. designed and performed experiments, analyzed the data, and wrote and revised the manuscript. B.G. performed experiments, analyzed data, and helped revise the manuscript. N.R. designed experiments and helped revise the paper. K.M designed experiments and wrote and revised the manuscript.

References

Abbott, A. L., Alvarez-Saavedra, E., Miska, E. A., Lau, N. C., Bartel, D. P., Horvitz, H. R., & Ambros, V. (2005). The let-7 MicroRNA family members mir-48, mir-84, and mir-241 function together to regulate developmental timing in Caenorhabditis elegans. *Developmental Cell*, *9*(3), 403–414. https://doi.org/10.1016/j.devcel.2005.07.009

Aboobaker, A. A., Tomancak, P., Patel, N., Rubin, G. M., & Lai, E. C. (2005). Drosophila microRNAs exhibit diverse spatial expression patterns during embryonic development. *Proceedings of the National Academy of Sciences of the United States of America*, *102*(50), 18017–18022. https://doi.org/10.1073/pnas.0508823102

Alberti, C., Manzenreither, R. A., Sowemimo, I., Burkard, T. R., Wang, J., Mahofsky, K., Ameres, S. L., & Cochella, L. (2018). Cell-type specific sequencing of microRNAs from complex animal tissues. *Nature Methods*, *15*(4), 283–289. https://doi.org/10.1038/nmeth.4610

Arribere, J. A., Bell, R. T., Fu, B. X., Artiles, K. L., Hartman, P. S., & Fire, A. Z. (2014). Efficient marker-free recovery of custom genetic modifications with CRISPR/Cas9 in Caenorhabditis elegans. *Genetics*, *198*(3), 837–846. https://doi.org/10.1534/genetics.114.169730

Auyeung, V. C., Ulitsky, I., McGeary, S. E., & Bartel, D. P. (2013). Beyond secondary structure: primary-sequence determinants license pri-miRNA hairpins for processing. *Cell*, *152*(4), 844–858. https://doi.org/10.1016/j.cell.2013.01.031

Banani, S. F., Lee, H. O., Hyman, A. A., & Rosen, M. K. (2017). Biomolecular condensates: organizers of cellular biochemistry. *Nature Reviews. Molecular Cell Biology*, *18*(5), 285–298. https://doi.org/10.1038/nrm.2017.7

Banani, S. F., Rice, A. M., Peeples, W. B., Lin, Y., Jain, S., Parker, R., & Rosen, M. K. (2016). Compositional Control of Phase-Separated Cellular Bodies. *Cell*, *166*(3), 651–663. https://doi.org/10.1016/j.cell.2016.06.010

Bartel, D. P. (2018). Metazoan MicroRNAs. In *Cell*. https://doi.org/10.1016/j.cell.2018.03.006

Bernstein, E., Caudy, A. A., Hammond, S. M., & Hannon, G. J. (2001). Role for a bidentate ribonuclease in the initiation step of RNA interference. *Nature*, *409*(6818), 363–366. https://doi.org/10.1038/35053110

Bindels, D. S., Haarbosch, L., van Weeren, L., Postma, M., Wiese, K. E., Mastop, M., Aumonier, S., Gotthard, G., Royant, A., Hink, M. A., & Gadella, T. W. J. (2017). mScarlet: a bright monomeric red fluorescent protein for cellular imaging. *Nature Methods*, *14*(1), 53–56. https://doi.org/10.1038/nmeth.4074

Bohnsack, M. T., Czaplinski, K., & Gorlich, D. (2004). Exportin 5 is a RanGTP-dependent dsRNA-binding protein that mediates nuclear export of pre-miRNAs. *RNA (New York, N.Y.)*, *10*(2), 185–191. https://doi.org/10.1261/rna.5167604

Brangwynne, C. P., Eckmann, C. R., Courson, D. S., Rybarska, A., Hoege, C., Gharakhani, J., Jülicher, F., & Hyman, A. A. (2009). Germline P granules are liquid droplets that localize by controlled dissolution/condensation. *Science (New York, N.Y.)*, *324*(5935), 1729–1732. https://doi.org/10.1126/science.1172046

Brosnan, C. A., Palmer, A. J., & Zuryn, S. (2021). Cell-type-specific profiling of loaded miRNAs from Caenorhabditis elegans reveals spatial and temporal flexibility in Argonaute loading. *Nature Communications*, *12*(1), 2194. https://doi.org/10.1038/s41467-021-22503-7

Büssing, I., Yang, J.-S., Lai, E. C., & Grosshans, H. (2010). The nuclear export receptor XPO-1 supports primary miRNA processing in C. elegans and Drosophila. *The EMBO Journal*, *29*(11), 1830–1839. https://doi.org/10.1038/emboj.2010.82

Cai, X., Hagedorn, C. H., & Cullen, B. R. (2004). Human microRNAs are processed from capped, polyadenylated transcripts that can also function as mRNAs. *RNA (New York, N.Y.)*, *10*(12), 1957–1966. https://doi.org/10.1261/rna.7135204

Chen, R. A.-J., Down, T. A., Stempor, P., Chen, Q. B., Egelhofer, T. A., Hillier, L. W., Jeffers, T. E., & Ahringer, J. (2013). The landscape of RNA polymerase II transcription initiation in C. elegans reveals promoter and enhancer architectures. *Genome Research*, *23*(8), 1339–1347. https://doi.org/10.1101/gr.153668.112

Chen, S. (2023). Ultrafast one-pass FASTQ data preprocessing, quality control, and deduplication using fastp. *IMeta*, *2*(2), e107. https://doi.org/10.1002/imt2.107

Clarke, A. W., Høye, E., Hembrom, A. A., Paynter, V. M., Vinther, J., Wyrożemski, Ł., Biryukova, I., Formaggioni, A., Ovchinnikov, V., Herlyn, H., Pierce, A., Wu, C., Aslanzadeh, M., Cheneby, J., Martinez, P., Friedländer, M. R., Hovig, E., Hackenberg, M., Umu, S. U., … Fromm, B. (2025). MirGeneDB 3.0: improved taxonomic sampling, uniform nomenclature of novel conserved microRNA families and updated covariance models. *Nucleic Acids Research*, *53*(D1), D116–D128. https://doi.org/10.1093/nar/gkae1094

Danecek, P., Bonfield, J. K., Liddle, J., Marshall, J., Ohan, V., Pollard, M. O., Whitwham, A., Keane, T., McCarthy, S. A., Davies, R. M., & Li, H. (2021). Twelve years of SAMtools and BCFtools. *GigaScience*, *10*(2). https://doi.org/10.1093/gigascience/giab008

Denli, A. M., Tops, B. B. J., Plasterk, R. H. A., Ketting, R. F., & Hannon, G. J. (2004). Processing of primary microRNAs by the Microprocessor complex. *Nature*, *432*(7014), 231–235. https://doi.org/10.1038/nature03049

Dexheimer, P. J., Wang, J., & Cochella, L. (2020). Two MicroRNAs Are Sufficient for Embryonic Patterning in C. elegans. *Current Biology*, *30*(24), 5058-5065.e5. https://doi.org/10.1016/j.cub.2020.09.066

Dignon, G. L., Best, R. B., & Mittal, J. (2020). Biomolecular Phase Separation: From Molecular Driving Forces to Macroscopic Properties. *Annual Review of Physical Chemistry*, *71*, 53–75. https://doi.org/10.1146/annurev-physchem-071819-113553

Donayo, A. O., Johnson, R. M., Tseng, H.-W., Izreig, S., Gariepy, A., Mayya, V. K., Wu, E., Alam, R., Lussier, C., Jones, R. G., & Duchaine, T. F. (2019). Oncogenic Biogenesis of pri-miR-17∼92 Reveals Hierarchy and Competition among Polycistronic MicroRNAs. *Molecular Cell*, *75*(2), 340-356.e10. https://doi.org/10.1016/j.molcel.2019.05.033

Donnelly, B. F., Yang, B., Grimme, A. L., Vieux, K.-F., Liu, C.-Y., Zhou, L., & McJunkin, K. (2022). The developmentally timed decay of an essential microRNA family is seed-sequence dependent. *Cell Reports*, *40*(6), 111154. https://doi.org/10.1016/j.celrep.2022.111154

Erdős, G., & Dosztányi, Z. (2020). Analyzing Protein Disorder with IUPred2A. *Current Protocols in Bioinformatics*, *70*(1), e99. https://doi.org/10.1002/cpbi.99

Fang, W., & Bartel, D. P. (2015). The Menu of Features that Define Primary MicroRNAs and Enable De Novo Design of MicroRNA Genes. *Molecular Cell*, *60*(1), 131–145. https://doi.org/10.1016/j.molcel.2015.08.015

Fang, W., & Bartel, D. P. (2020). MicroRNA Clustering Assists Processing of Suboptimal MicroRNA Hairpins through the Action of the ERH Protein. *Molecular Cell*, *78*(2), 289-302.e6. https://doi.org/10.1016/j.molcel.2020.01.026

641 Frøkjaer-Jensen, C., Davis, M. W., Hopkins, C. E., Newman, B. J., Thummel, J. M., Olesen, S.-
642 P., Grunnet, M., & Jorgensen, E. M. (2008). Single-copy insertion of transgenes in
643 Caenorhabditis elegans. *Nature Genetics*, *40*(11), 1375–1383.
644 https://doi.org/10.1038/ng.248
645 Fromm, B., Billipp, T., Peck, L. E., Johansen, M., Tarver, J. E., King, B. L., Newcomb, J. M.,
646 Sempere, L. F., Flatmark, K., Hovig, E., & Peterson, K. J. (2015). A Uniform System for the
647 Annotation of Vertebrate microRNA Genes and the Evolution of the Human
648 microRNAome. *Annual Review of Genetics*, *49*, 213–242. https://doi.org/10.1146/annurev-
649 genet-120213-092023
650 Garg, A., Shang, R., Cvetanovic, T., Lai, E. C., & Joshua-Tor, L. (2024). The structural landscape
651 of Microprocessor-mediated processing of pri-let-7 miRNAs. *Molecular Cell*, *84*(21), 4175-
652 4190.e6. https://doi.org/10.1016/j.molcel.2024.09.008
653 Gregory, R. I., Chendrimada, T. P., Cooch, N., & Shiekhattar, R. (2005). Human RISC couples
654 microRNA biogenesis and posttranscriptional gene silencing. *Cell*, *123*(4), 631–640.
655 https://doi.org/10.1016/j.cell.2005.10.022
656 Gregory, R. I., Yan, K.-P., Amuthan, G., Chendrimada, T., Doratotaj, B., Cooch, N., &
657 Shiekhattar, R. (2004). The Microprocessor complex mediates the genesis of microRNAs.
658 *Nature*, *432*(7014), 235–240. https://doi.org/10.1038/nature03120
659 Grishok, A., Pasquinelli, A. E., Conte, D., Li, N., Parrish, S., Ha, I., Baillie, D. L., Fire, A.,
660 Ruvkun, G., & Mello, C. C. (2001). Genes and mechanisms related to RNA interference
661 regulate expression of the small temporal RNAs that control C. elegans developmental
662 timing. *Cell*, *106*(1), 23–34. https://doi.org/10.1016/s0092-8674(01)00431-7
663 Gu, W., Lee, H.-C., Chaves, D., Youngman, E. M., Pazour, G. J., Conte, D., & Mello, C. C.
664 (2012). CapSeq and CIP-TAP identify Pol II start sites and reveal capped small RNAs as C.
665 elegans piRNA precursors. *Cell*, *151*(7), 1488–1500.
666 https://doi.org/10.1016/j.cell.2012.11.023
667 Hammond, S. M., Boettcher, S., Caudy, A. A., Kobayashi, R., & Hannon, G. J. (2001).
668 Argonaute2, a link between genetic and biochemical analyses of RNAi. *Science (New York,*
669 *N.Y.)*, *293*(5532), 1146–1150. https://doi.org/10.1126/science.1064023
670 Han, J., Lee, Y., Yeom, K.-H., Kim, Y.-K., Jin, H., & Kim, V. N. (2004). The Drosha-DGCR8
671 complex in primary microRNA processing. *Genes & Development*, *18*(24), 3016–3027.
672 https://doi.org/10.1101/gad.1262504
673 Han, J., Lee, Y., Yeom, K.-H., Nam, J.-W., Heo, I., Rhee, J.-K., Sohn, S. Y., Cho, Y., Zhang, B.-
674 T., & Kim, V. N. (2006). Molecular basis for the recognition of primary microRNAs by the
675 Drosha-DGCR8 complex. *Cell*, *125*(5), 887–901. https://doi.org/10.1016/j.cell.2006.03.043
676 Hills-Muckey, K., Martinez, M. A. Q., Stec, N., Hebbar, S., Saldanha, J., Medwig-Kinney, T. N.,
677 Moore, F. E. Q., Ivanova, M., Morao, A., Ward, J. D., Moss, E. G., Ercan, S., Zinovyeva, A.
678 Y., Matus, D. Q., & Hammell, C. M. (2022). An engineered, orthogonal auxin
679 analog/AtTIR1(F79G) pairing improves both specificity and efficacy of the auxin
680 degradation system in Caenorhabditis elegans. *Genetics*, *220*(2).
681 https://doi.org/10.1093/genetics/iyab174
682 Hutter, K., Lohmüller, M., Jukic, A., Eichin, F., Avci, S., Labi, V., Szabo, T. G., Hoser, S. M.,
683 Hüttenhofer, A., Villunger, A., & Herzog, S. (2020). SAFB2 Enables the Processing of
684 Suboptimal Stem-Loop Structures in Clustered Primary miRNA Transcripts. *Molecular*
685 *Cell*, *78*(5), 876-889.e6. https://doi.org/10.1016/j.molcel.2020.05.011

Hutvágner, G., McLachlan, J., Pasquinelli, A. E., Bálint, E., Tuschl, T., & Zamore, P. D. (2001). A cellular function for the RNA-interference enzyme Dicer in the maturation of the let-7 small temporal RNA. *Science (New York, N.Y.)*, *293*(5531), 834–838. https://doi.org/10.1126/science.1062961

Janas, M. M., Khaled, M., Schubert, S., Bernstein, J. G., Golan, D., Veguilla, R. A., Fisher, D. E., Shomron, N., Levy, C., & Novina, C. D. (2011). Feed-forward microprocessing and splicing activities at a microRNA-containing intron. *PLoS Genetics*, *7*(10), e1002330. https://doi.org/10.1371/journal.pgen.1002330

Jiang, L., Shao, C., Wu, Q.-J., Chen, G., Zhou, J., Yang, B., Li, H., Gou, L.-T., Zhang, Y., Wang, Y., Yeo, G. W., Zhou, Y., & Fu, X.-D. (2017). NEAT1 scaffolds RNA-binding proteins and the Microprocessor to globally enhance pri-miRNA processing. *Nature Structural & Molecular Biology*, *24*(10), 816–824. https://doi.org/10.1038/nsmb.3455

Jin, W., Wang, J., Liu, C.-P., Wang, H.-W., & Xu, R.-M. (2020). Structural Basis for pri-miRNA Recognition by Drosha. *Molecular Cell*, *78*(3), 423-433.e5. https://doi.org/10.1016/j.molcel.2020.02.024

Ketting, R. F., Fischer, S. E., Bernstein, E., Sijen, T., Hannon, G. J., & Plasterk, R. H. (2001). Dicer functions in RNA interference and in synthesis of small RNA involved in developmental timing in C. elegans. *Genes & Development*, *15*(20), 2654–2659. https://doi.org/10.1101/gad.927801

Kim, B., Jeong, K., & Kim, V. N. (2017). Genome-wide Mapping of DROSHA Cleavage Sites on Primary MicroRNAs and Noncanonical Substrates. *Molecular Cell*, *66*(2), 258-269.e5. https://doi.org/10.1016/j.molcel.2017.03.013

Kim, H., Lee, Y.-Y., & Kim, V. N. (2024). The biogenesis and regulation of animal microRNAs. *Nature Reviews. Molecular Cell Biology*. https://doi.org/10.1038/s41580-024-00805-0

Knight, S. W., & Bass, B. L. (2001). A role for the RNase III enzyme DCR-1 in RNA interference and germ line development in Caenorhabditis elegans. *Science (New York, N.Y.)*, *293*(5538), 2269–2271. https://doi.org/10.1126/science.1062039

Kotagama, K., Grimme, A. L., Braviner, L., Yang, B., Sakhawala, R. M., Yu, G., Benner, L. K., Joshua-Tor, L., & McJunkin, K. (2024). Catalytic residues of microRNA Argonautes play a modest role in microRNA star strand destabilization in C. elegans. *Nucleic Acids Research*, *52*(9), 4985–5001. https://doi.org/10.1093/nar/gkae170

Kruesi, W. S., Core, L. J., Waters, C. T., Lis, J. T., & Meyer, B. J. (2013). Condensin controls recruitment of RNA polymerase II to achieve nematode X-chromosome dosage compensation. *ELife*, *2*, e00808. https://doi.org/10.7554/eLife.00808

Kwon, S. C., Baek, S. C., Choi, Y.-G., Yang, J., Lee, Y.-S., Woo, J.-S., & Kim, V. N. (2019). Molecular Basis for the Single-Nucleotide Precision of Primary microRNA Processing. *Molecular Cell*, *73*(3), 505-518.e5. https://doi.org/10.1016/j.molcel.2018.11.005

Kwon, S. C., Nguyen, T. A., Choi, Y.-G., Jo, M. H., Hohng, S., Kim, V. N., & Woo, J.-S. (2016). Structure of Human DROSHA. *Cell*, *164*(1–2), 81–90. https://doi.org/10.1016/j.cell.2015.12.019

Landgraf, P., Rusu, M., Sheridan, R., Sewer, A., Iovino, N., Aravin, A., Pfeffer, S., Rice, A., Kamphorst, A. O., Landthaler, M., Lin, C., Socci, N. D., Hermida, L., Fulci, V., Chiaretti, S., Foà, R., Schliwka, J., Fuchs, U., Novosel, A., … Tuschl, T. (2007). A mammalian microRNA expression atlas based on small RNA library sequencing. *Cell*, *129*(7), 1401–1414. https://doi.org/10.1016/j.cell.2007.04.040

Landthaler, M., Yalcin, A., & Tuschl, T. (2004). The human DiGeorge syndrome critical region gene 8 and Its D. melanogaster homolog are required for miRNA biogenesis. *Current Biology : CB*, *14*(23), 2162–2167. https://doi.org/10.1016/j.cub.2004.11.001

Langmead, B., & Salzberg, S. L. (2012). Fast gapped-read alignment with Bowtie 2. *Nature Methods*, *9*(4), 357–359. https://doi.org/10.1038/nmeth.1923

Lataniotis, L., Albrecht, A., Kok, F. O., Monfries, C. A. L., Benedetti, L., Lawson, N. D., Hughes, S. M., Steinhofel, K., Mayr, M., & Zampetaki, A. (2017). CRISPR/Cas9 editing reveals novel mechanisms of clustered microRNA regulation and function. *Scientific Reports*, *7*(1), 8585. https://doi.org/10.1038/s41598-017-09268-0

Lee, Y., Ahn, C., Han, J., Choi, H., Kim, J., Yim, J., Lee, J., Provost, P., Rådmark, O., Kim, S., & Kim, V. N. (2003). The nuclear RNase III Drosha initiates microRNA processing. *Nature*, *425*(6956), 415–419. https://doi.org/10.1038/nature01957

Lee, Y., Kim, M., Han, J., Yeom, K.-H., Lee, S., Baek, S. H., & Kim, V. N. (2004). MicroRNA genes are transcribed by RNA polymerase II. *The EMBO Journal*, *23*(20), 4051–4060. https://doi.org/10.1038/sj.emboj.7600385

Li, S., Nguyen, T. D., Nguyen, T. L., & Nguyen, T. A. (2020). Mismatched and wobble base pairs govern primary microRNA processing by human Microprocessor. *Nature Communications*, *11*(1), 1926. https://doi.org/10.1038/s41467-020-15674-2

Li, S., Nguyen, T. D., Nguyen, T. L., & Nguyen, T. A. (2021). Author Correction: Mismatched and wobble base pairs govern primary microRNA processing by human Microprocessor. *Nature Communications*, *12*(1), 6255. https://doi.org/10.1038/s41467-021-26533-z

Love, M. I., Huber, W., & Anders, S. (2014). Moderated estimation of fold change and dispersion for RNA-seq data with DESeq2. *Genome Biology*, *15*(12), 550. https://doi.org/10.1186/s13059-014-0550-8

Lund, E., Güttinger, S., Calado, A., Dahlberg, J. E., & Kutay, U. (2004). Nuclear export of microRNA precursors. *Science (New York, N.Y.)*, *303*(5654), 95–98. https://doi.org/10.1126/science.1090599

Martinez, N. J., Ow, M. C., Reece-Hoyes, J. S., Barrasa, M. I., Ambros, V. R., & Walhout, A. J. M. (2008). Genome-scale spatiotemporal analysis of Caenorhabditis elegans microRNA promoter activity. *Genome Research*, *18*(12), 2005–2015. https://doi.org/10.1101/gr.083055.108

Merritt, C., Rasoloson, D., Ko, D., & Seydoux, G. (2008). 3' UTRs are the primary regulators of gene expression in the C. elegans germline. *Current Biology : CB*, *18*(19), 1476–1482. https://doi.org/10.1016/j.cub.2008.08.013

Mészáros, B., Erdos, G., & Dosztányi, Z. (2018). IUPred2A: context-dependent prediction of protein disorder as a function of redox state and protein binding. *Nucleic Acids Research*, *46*(W1), W329–W337. https://doi.org/10.1093/nar/gky384

Mitrea, D. M., & Kriwacki, R. W. (2016). Phase separation in biology; functional organization of a higher order. *Cell Communication and Signaling : CCS*, *14*, 1. https://doi.org/10.1186/s12964-015-0125-7

Mourelatos, Z., Dostie, J., Paushkin, S., Sharma, A., Charroux, B., Abel, L., Rappsilber, J., Mann, M., & Dreyfuss, G. (2002). miRNPs: a novel class of ribonucleoproteins containing numerous microRNAs. *Genes & Development*, *16*(6), 720–728. https://doi.org/10.1101/gad.974702

Nguyen, T. A., Jo, M. H., Choi, Y.-G., Park, J., Kwon, S. C., Hohng, S., Kim, V. N., & Woo, J.-S. (2015). Functional Anatomy of the Human Microprocessor. *Cell*, *161*(6), 1374–1387. https://doi.org/10.1016/j.cell.2015.05.010

Nguyen, T. L., Nguyen, T. D., Ngo, M. K., Le, T. N.-Y., & Nguyen, T. A. (2023). Noncanonical processing by animal Microprocessor. *Molecular Cell*, *83*(11), 1810-1826.e8. https://doi.org/10.1016/j.molcel.2023.05.004

Nguyen, T. L., Nguyen, T. D., Ngo, M. K., & Nguyen, T. A. (2023). Dissection of the Caenorhabditis elegans Microprocessor. *Nucleic Acids Research*, *51*(4), 1512–1527. https://doi.org/10.1093/nar/gkac1170

Paix, A., Wang, Y., Smith, H. E., Lee, C. Y. S., Calidas, D., Lu, T., Smith, J., Schmidt, H., Krause, M. W., & Seydoux, G. (2014). Scalable and versatile genome editing using linear DNAs with microhomology to Cas9 sites in Caenorhabditis elegans. *Genetics*, *198*(4), 1347–1356. https://doi.org/10.1534/genetics.114.170423

Partin, A. C., Ngo, T. D., Herrell, E., Jeong, B.-C., Hon, G., & Nam, Y. (2017). Heme enables proper positioning of Drosha and DGCR8 on primary microRNAs. *Nature Communications*, *8*(1), 1737. https://doi.org/10.1038/s41467-017-01713-y

Partin, A. C., Zhang, K., Jeong, B.-C., Herrell, E., Li, S., Chiu, W., & Nam, Y. (2020). Cryo-EM Structures of Human Drosha and DGCR8 in Complex with Primary MicroRNA. *Molecular Cell*, *78*(3), 411-422.e4. https://doi.org/10.1016/j.molcel.2020.02.016

Pawlicki, J. M., & Steitz, J. A. (2008). Primary microRNA transcript retention at sites of transcription leads to enhanced microRNA production. *The Journal of Cell Biology*, *182*(1), 61–76. https://doi.org/10.1083/jcb.200803111

Pham, K., Masoudi, N., Leyva-Díaz, E., & Hobert, O. (2021). A nervous system-specific subnuclear organelle in Caenorhabditis elegans. *Genetics*, *217*(1), 1–17. https://doi.org/10.1093/genetics/iyaa016

Piuco, R., & Galante, P. A. F. (2021). *piRNAdb: A piwi-interacting RNA database*. https://doi.org/10.1101/2021.09.21.461238

Prabhakar, A., Hu, S., Tang, J., Ghatpande, P., Lagna, G., Jiang, X., & Hata, A. (2023). Essential role of the amino-terminal region of Drosha for the Microprocessor function. *IScience*, *26*(10), 107971. https://doi.org/10.1016/j.isci.2023.107971

Putnam, A., Thomas, L., & Seydoux, G. (2023). RNA granules: functional compartments or incidental condensates? *Genes & Development*, *37*(9–10), 354–376. https://doi.org/10.1101/gad.350518.123

Putri, G. H., Anders, S., Pyl, P. T., Pimanda, J. E., & Zanini, F. (2022). Analysing high-throughput sequencing data in Python with HTSeq 2.0. *Bioinformatics (Oxford, England)*, *38*(10), 2943–2945. https://doi.org/10.1093/bioinformatics/btac166

Reinhart, B. J., Slack, F. J., Basson, M., Pasquinelli, A. E., Bettinger, J. C., Rougvie, A. E., Horvitz, H. R., & Ruvkun, G. (2000). The 21-nucleotide let-7 RNA regulates developmental timing in Caenorhabditis elegans. *Nature*, *403*(6772), 901–906. https://doi.org/10.1038/35002607

Saito, T. L., Hashimoto, S., Gu, S. G., Morton, J. J., Stadler, M., Blumenthal, T., Fire, A., & Morishita, S. (2013). The transcription start site landscape of C. elegans. *Genome Research*, *23*(8), 1348–1361. https://doi.org/10.1101/gr.151571.112

Shang, R., Baek, S. C., Kim, K., Kim, B., Kim, V. N., & Lai, E. C. (2020). Genomic Clustering Facilitates Nuclear Processing of Suboptimal Pri-miRNA Loci. *Molecular Cell*, *78*(2), 303-316.e4. https://doi.org/10.1016/j.molcel.2020.02.009

Slack, F. J., Basson, M., Liu, Z., Ambros, V., Horvitz, H. R., & Ruvkun, G. (2000). The lin-41 RBCC gene acts in the C. elegans heterochronic pathway between the let-7 regulatory RNA and the LIN-29 transcription factor. *Molecular Cell*, *5*(4), 659–669. https://doi.org/10.1016/s1097-2765(00)80245-2

Slezak-Prochazka, I., Kluiver, J., de Jong, D., Kortman, G., Halsema, N., Poppema, S., Kroesen, B.-J., & van den Berg, A. (2013). Cellular localization and processing of primary transcripts of exonic microRNAs. *PloS One*, *8*(9), e76647. https://doi.org/10.1371/journal.pone.0076647

Son, S., Kim, B., Yang, J., & Kim, V. N. (2023). Role of the proline-rich disordered domain of DROSHA in intronic microRNA processing. *Genes & Development*, *37*(9–10), 383–397. https://doi.org/10.1101/gad.350275.122

Sternberg, P. W., Van Auken, K., Wang, Q., Wright, A., Yook, K., Zarowiecki, M., Arnaboldi, V., Becerra, A., Brown, S., Cain, S., Chan, J., Chen, W. J., Cho, J., Davis, P., Diamantakis, S., Dyer, S., Grigoriadis, D., Grove, C. A., Harris, T., … Stein, L. (2024). WormBase 2024: status and transitioning to Alliance infrastructure. *Genetics*, *227*(1). https://doi.org/10.1093/genetics/iyae050

Stiernagle, T. (2006). Maintenance of C. elegans. *WormBook : The Online Review of C. Elegans Biology*, 1–11. https://doi.org/10.1895/wormbook.1.101.1

Tabara, H., Sarkissian, M., Kelly, W. G., Fleenor, J., Grishok, A., Timmons, L., Fire, A., & Mello, C. C. (1999). The rde-1 gene, RNA interference, and transposon silencing in C. elegans. *Cell*, *99*(2), 123–132. https://doi.org/10.1016/s0092-8674(00)81644-x

Thivierge, C., Bellefeuille, M., Diwan, S.-S., Dyakov, B. J. A., Leventis, R., Perron, G., Najafabadi, H. S., Gravel, S.-P., Gingras, A.-C., & Duchaine, T. F. (2024). Paraspeckle-independent co-transcriptional regulation of nuclear microRNA biogenesis by SFPQ. *Cell Reports*, *43*(9), 114695. https://doi.org/10.1016/j.celrep.2024.114695

Truscott, M., Islam, A. B. M. M. K., & Frolov, M. V. (2016). Novel regulation and functional interaction of polycistronic miRNAs. *RNA (New York, N.Y.)*, *22*(1), 129–138. https://doi.org/10.1261/rna.053264.115

Vieux, K.-F., Prothro, K. P., Kelley, L. H., Palmer, C., Maine, E. M., Veksler-Lublinsky, I., & McJunkin, K. (2021). Screening by deep sequencing reveals mediators of microRNA tailing in C. elegans. *Nucleic Acids Research*, *49*(19), 11167–11180. https://doi.org/10.1093/nar/gkab840

Witten, G., DeMott, E., Huang, G., Zelasko, F., de Jesus, B., Mulchand, C., Schuck, L., Pullman, S., Perez, A., Mahableshwarkar, P., Wu, Z., Cardona, E. A., Pierce, J. T., Dickinson, D. J., & Doonan, R. (2023). mScarlet and split fluorophore mScarlet resources for plasmid-based CRISPR/Cas9 knock-in in C. elegans. *MicroPublication Biology*, *2023*. https://doi.org/10.17912/micropub.biology.000871

Yang, B., Schwartz, M., & McJunkin, K. (2020). In vivo CRISPR screening for phenotypic targets of the mir-35-42 family in C. elegans. *Genes & Development* , *34*(17–18), 1227–1238. https://doi.org/10.1101/gad.339333.120

Yi, R., Qin, Y., Macara, I. G., & Cullen, B. R. (2003). Exportin-5 mediates the nuclear export of pre-microRNAs and short hairpin RNAs. *Genes & Development*, *17*(24), 3011–3016. https://doi.org/10.1101/gad.1158803

Zeng, Y., & Cullen, B. R. (2004). Structural requirements for pre-microRNA binding and nuclear export by Exportin 5. *Nucleic Acids Research*, *32*(16), 4776–4785. https://doi.org/10.1093/nar/gkh824

Zeng, Y., Yi, R., & Cullen, B. R. (2005). Recognition and cleavage of primary microRNA precursors by the nuclear processing enzyme Drosha. *The EMBO Journal*, *24*(1), 138–148. https://doi.org/10.1038/sj.emboj.7600491

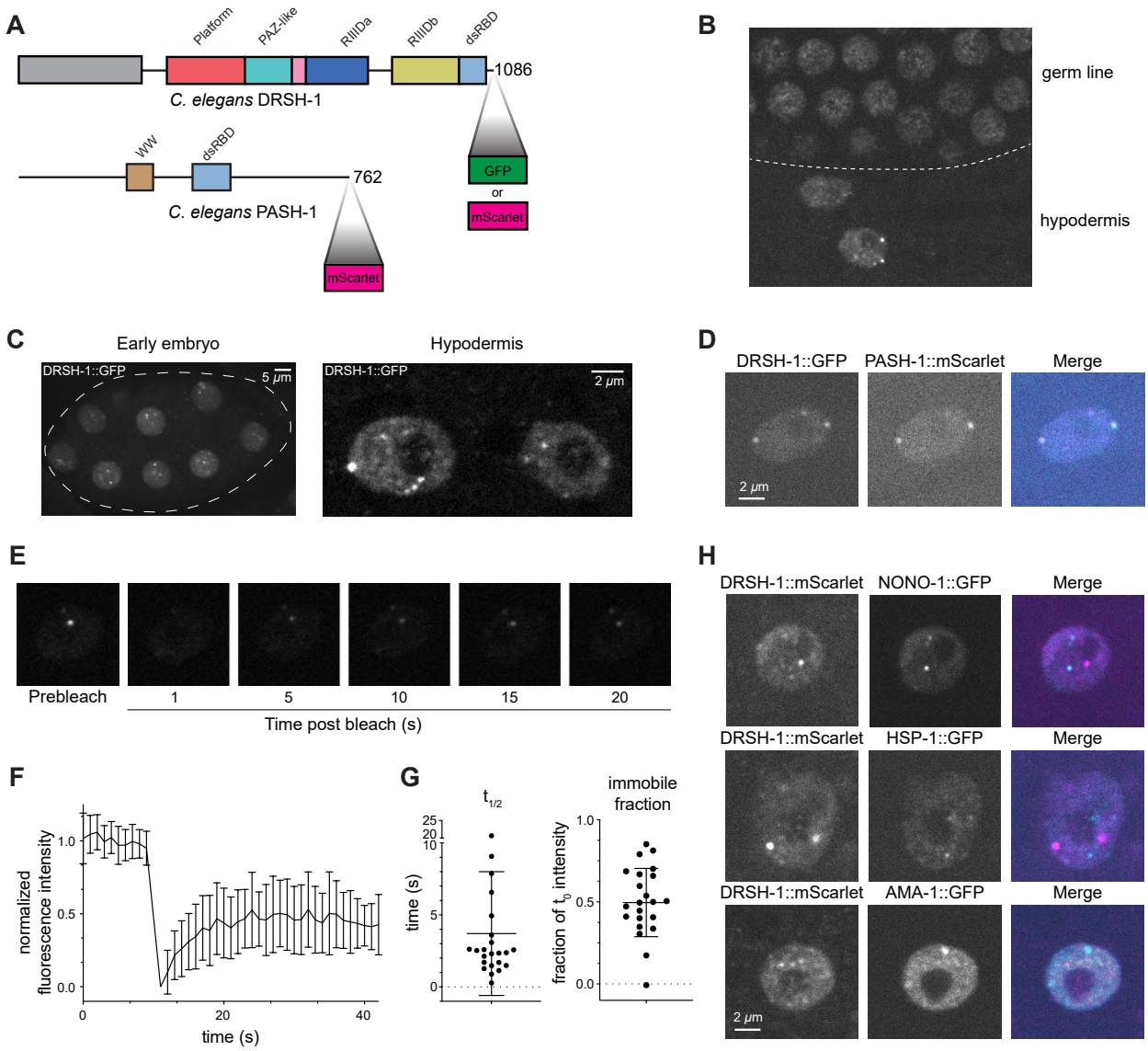

Figure 1. Microprocessor forms distinct nuclear granules in select tissues. (A) Domain architecture of *C. elegans* DRSH-1 and PASH-1. GFP and mScarlet were fused to DRSH-1 and PASH-1 at the C-terminus endogenously via CRISPR/Cas9. RIIID = RNase III domain, dsRBD = dsRNA binding domain. (B) Micrograph showing DRSH-1::GFP in germline nuclei lacking foci (top) and hypodermis nuclei containing foci (bottom). (C) Representative micrographs of DRSH-1::GFP in early embryos (left) and two hypodermal nuclei (right). Left: Dotted line outlines the embryo structure. Right: The large nucleoli characteristic of hypodermal nuclei exclude DRSH-1::GFP. Maximum intensity projection. (D) Representative images of co-localization of DRSH-1::GFP and PASH-1::mScarlet in a hypodermal cell. Single z plane shown. (E) Time-lapse images show fluorescence recovery of DRSH-1::GFP after a single *focus* is photobleached at 1.0 sec. Single z plane shown (F) FRAP recovery curves for DRSH-1::GFP. Data is reported as a mean +/- SD (n = 23 granules). (G) Half recovery time and immobile fraction were calculated based on fitted FRAP recovery curves for individual foci as shown in figure E. Bars are mean +/- SD. (H)

Representative images show co-labeling of DRSH-1::GFP and known nuclear granule markers. Maximum intensity projections.

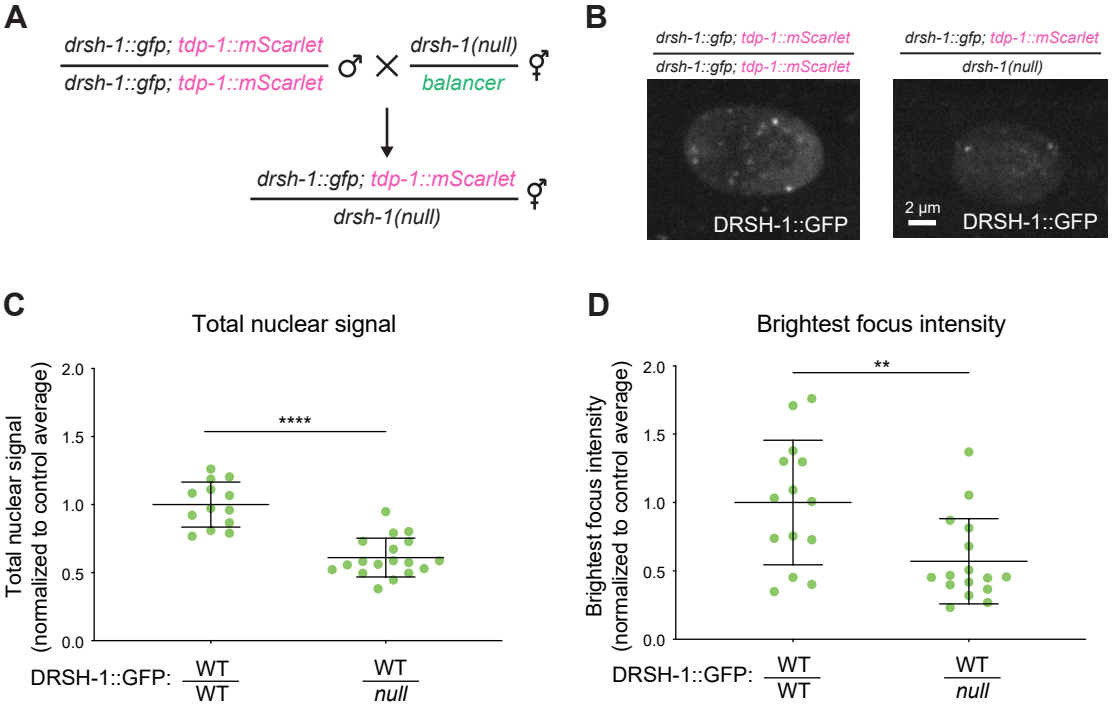

Figure 2. DRSH-1 granules are not strictly dependent on saturation concentration of DRSH-1. (A) Schematic of the genetic cross to generate *drsh-1::gfp/drsh-1(null)* heterozygous. *tdp-1::mScarlet* is a visual marker to differentiate cross progeny from self-progeny. Heterozygous worms were selected based on the visual marker. *drsh-1::gfp;tdp-1::mScarlet* homozygous worms were collected and used as control. (B) Representative images of DRSH-1::GFP in hypodermal cells in genetic background containing two (left) or one (right) allele of DRSH-1::GFP. Maximum intensity projection. (C) Quantification of the total nuclear signal of DRSH-1::GFP. (D) Quantification of the signal intensity of the brightest focus per nucleus across indicated genotypes in hypodermal cells. (C-D) Signal is normalized to the average signal in the control genotype (homozygous DRSH-1::GFP).

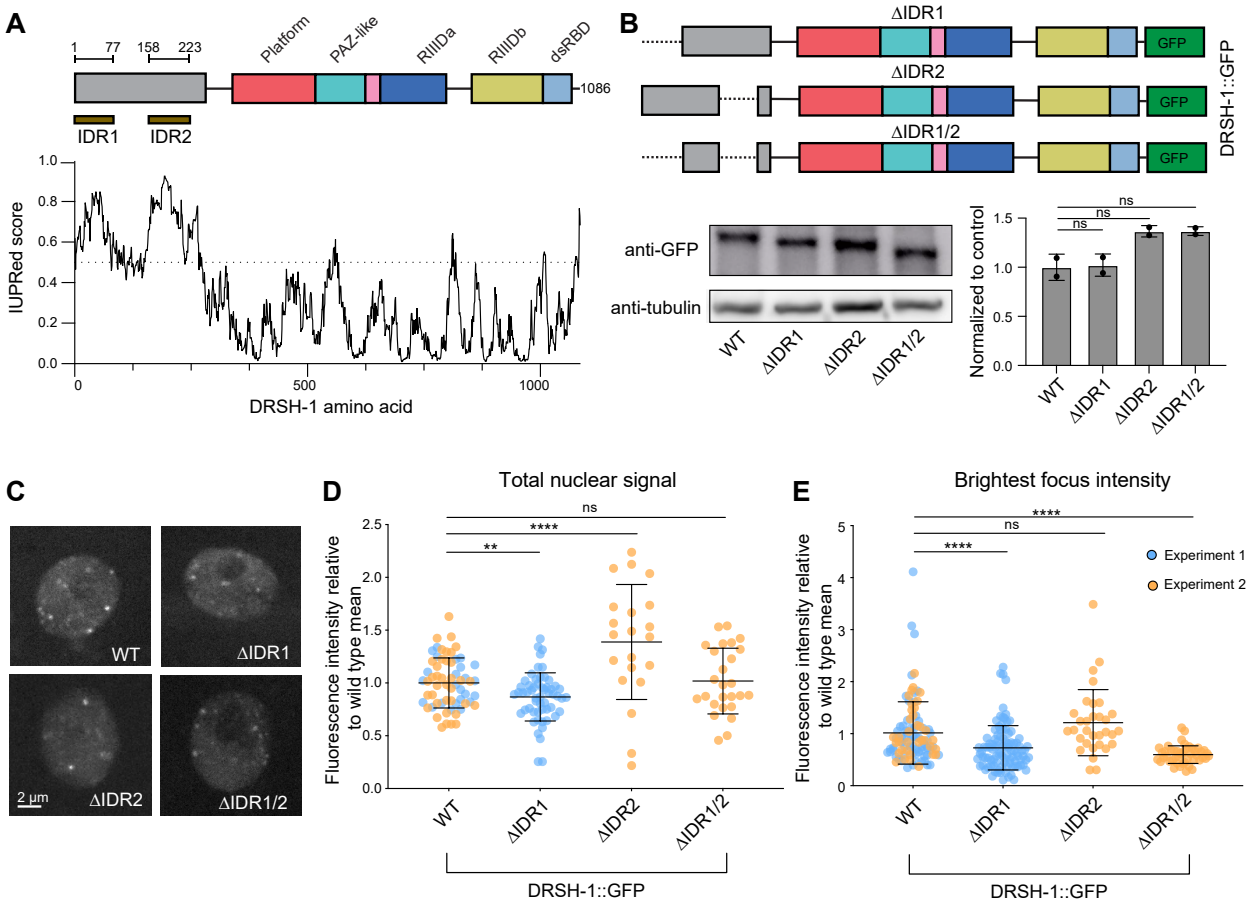

Figure 3. Deletion of N-terminal IDRs reduces but does not abolish DRSH-1 granule recruitment. (A) IUPRed was used to predict two intrinsically disordered domains: IDR1 (A.A. 1-77) and IDR2 (A.A. 158-233). (B) Schematics of IDR deletions generated in the *drsh-1::gfp* background using CRISPR/Cas9 and representative western blot images to show truncations of the DRSH-1::GFP fusion proteins in whole animal samples. Western quantification was normalized first to tubulin and then compared to wild type. Two tailed unpaired Student's test: ns, not significant. (C) Representative images of DRSH-1::GFP signal in hypodermal nuclei across different genotypes. Maximum intensity projections. (D) Super plot showing the quantification of total nuclear signal of DRSH-1::GFP. (E) Super plot showing the quantification of the intensity of the brightest focus in each nucleus. (D-E) Signal is normalized to the average signal in the control genotype (wild type DRSH-1::GFP) from the same imaging session. Data are color-coded by imaging session.

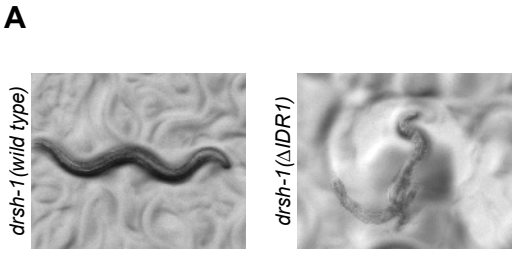

B

	number burst animals	n	percent bursting
drsh-1(wild type)	0	100	0.0%
drsh-1(ΔIDR1)	55	599	9.2%
drsh-1(ΔIDR2)	0	289	0.0%
drsh-1::gfp(wild type)	0	234	0.0%
drsh-1::gfp(ΔIDR1)	24	228	10.5%
drsh-1::gfp(ΔIDR2)	0	331	0.0%
drsh-1::gfp(ΔIDR1/2)	18	184	9.8%

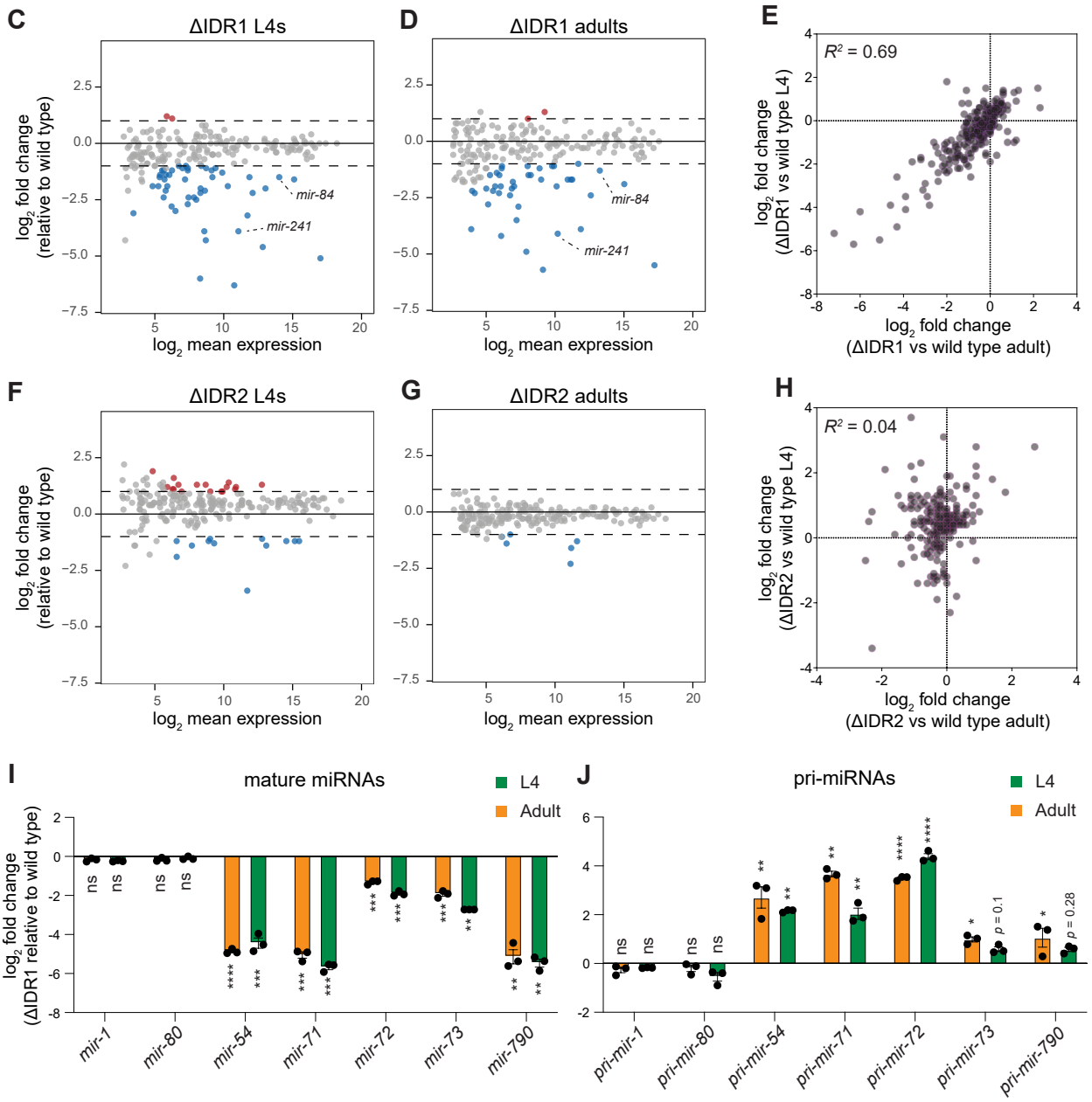

Figure 4. DRSH-1 IDR1 is important for the biogenesis of a subset of miRNAs. (A) Representative images showing the bursting phenotypes observed in ΔIDR1 young adult animals. (B) Table listing the penetrance of the bursting phenotype in different genotypes. IDR deletions

927 were generated in both N2 and *drsh-1::gfp* backgrounds. (C-D, F-G) MA plots showing average
928 abundance on the X-axis and the log_2fold change on the Y-axis. Sequencing analysis results were
929 obtained from DESeq2 using total piRNA reads for normalization. miRNAs showing significant
930 changes compared to wild type of the same stage are shown in blue (downregulated, log_2fold
931 change < -1 and $p_{adj} < 0.05$) and red (upregulated, log_2fold change > 1 and $p_{adj} < 0.05$ (C and D)
932 MA plots showing miRNA abundance changes in ΔIDR1 versus wild type for L4 and adult,
933 respectively (E) X-Y plot showing the correlation of log_2fold change for ΔIDR1/wild type between
934 L4 (Y-axis) and adult (X-axis). (F and G) MA plots showing miRNA abundance changes in ΔIDR2
935 versus wild type for L4 and adult, respectively. (H) X-Y plot showing the correlation of log_2fold
936 change for ΔIDR2/wild type between L4 and adult samples. (I) Relative levels of mature miRNAs
937 as measured by Taqman qPCR in ΔIDR1 L4 and adults, normalized to wild type of the same stage.
938 (J) Relative levels of primary miRNA transcripts as measured by qRT-PCR in ΔIDR1 L4 and adults,
939 normalized to wild type of the same stage. (I-J) *Sn2429* and *gpd-1* were used as internal controls
940 for mature miRNAs and pri-miRNAs, respectively. Two tailed unpaired Student's test: (*) P <
941 0.05, (**) P < 0.01, (***) P < 0.001, (****) P < 0.0001.
942

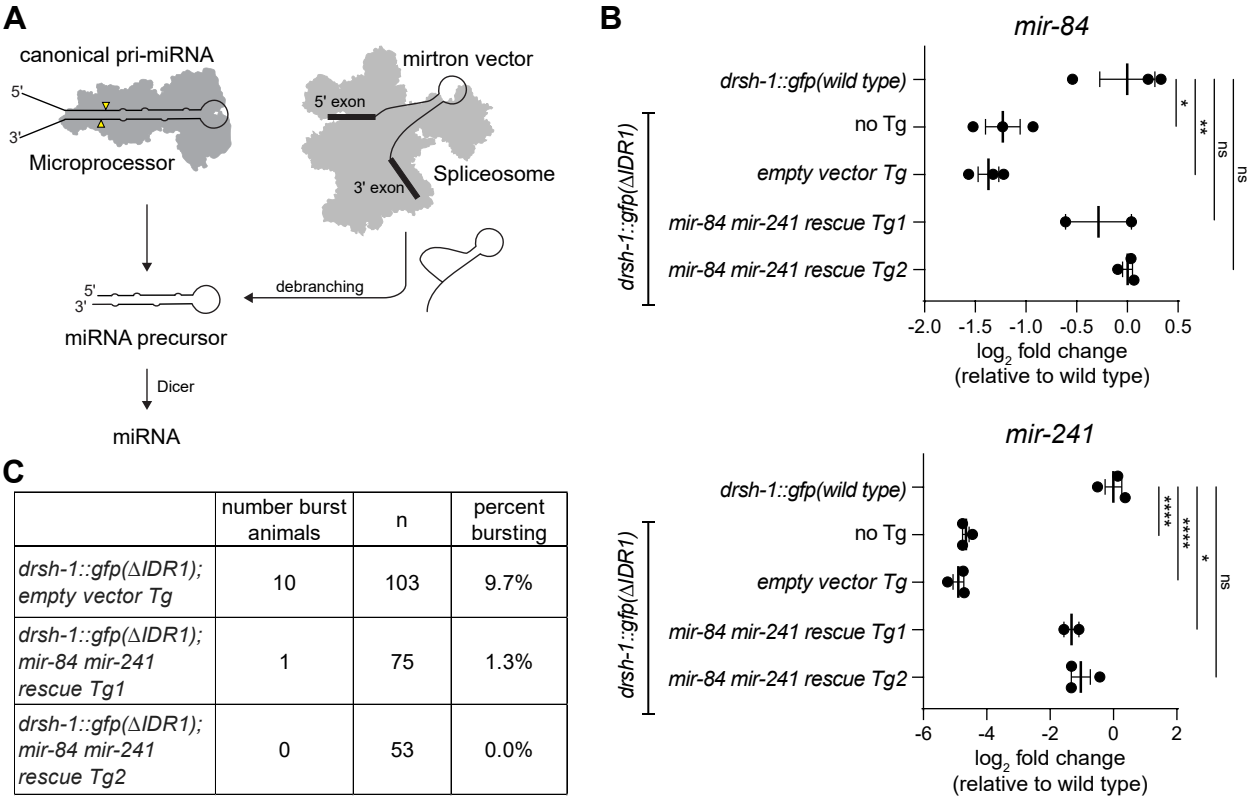

C

	number burst animals	n	percent bursting
drsh-1::gfp(ΔIDR1); empty vector Tg	10	103	9.7%
drsh-1::gfp(ΔIDR1); mir-84 mir-241 rescue Tg1	1	75	1.3%
drsh-1::gfp(ΔIDR1); mir-84 mir-241 rescue Tg2	0	53	0.0%

Figure 5. Microprocessor-independent miRNA expression rescues DRSH-1 ΔIDR1 bursting phenotype. (A) Schematic of the *mir-84* and *mir-241* mirtron design strategy. On the left is the canonical miRNA processing pathway that involves the Microprocessor; the right shows the mirtron embedded between two exons of a GFP minigene. Splicing of the mirtron-containing intron, followed by debranching of the intron lariat, allows miRNA precursor production independent of Microprocessor. (B) *mir-84* and *mir-241* expression levels measured by Taqman qPCR. *Sn2429* was used as internal control, and wild type was used as the normalization group. Two tailed unpaired Student's t-test: (*) $p < 0.05$, (**) $p < 0.01$, (***) $p < 0.001$, (****) $p < 0.0001$. (C) Table listing the penetrance of the bursting phenotype in different genotypes. *Mir-84 mir-241* rescue Tg1 and Tg2 are two independent extrachromosomal arrays carrying the mirtron vectors. The empty vector control Tg contains all coinjection markers used in the mirtron Tgs as well as the empty plasmid backbone used for cloning the mirtron expression fragments.

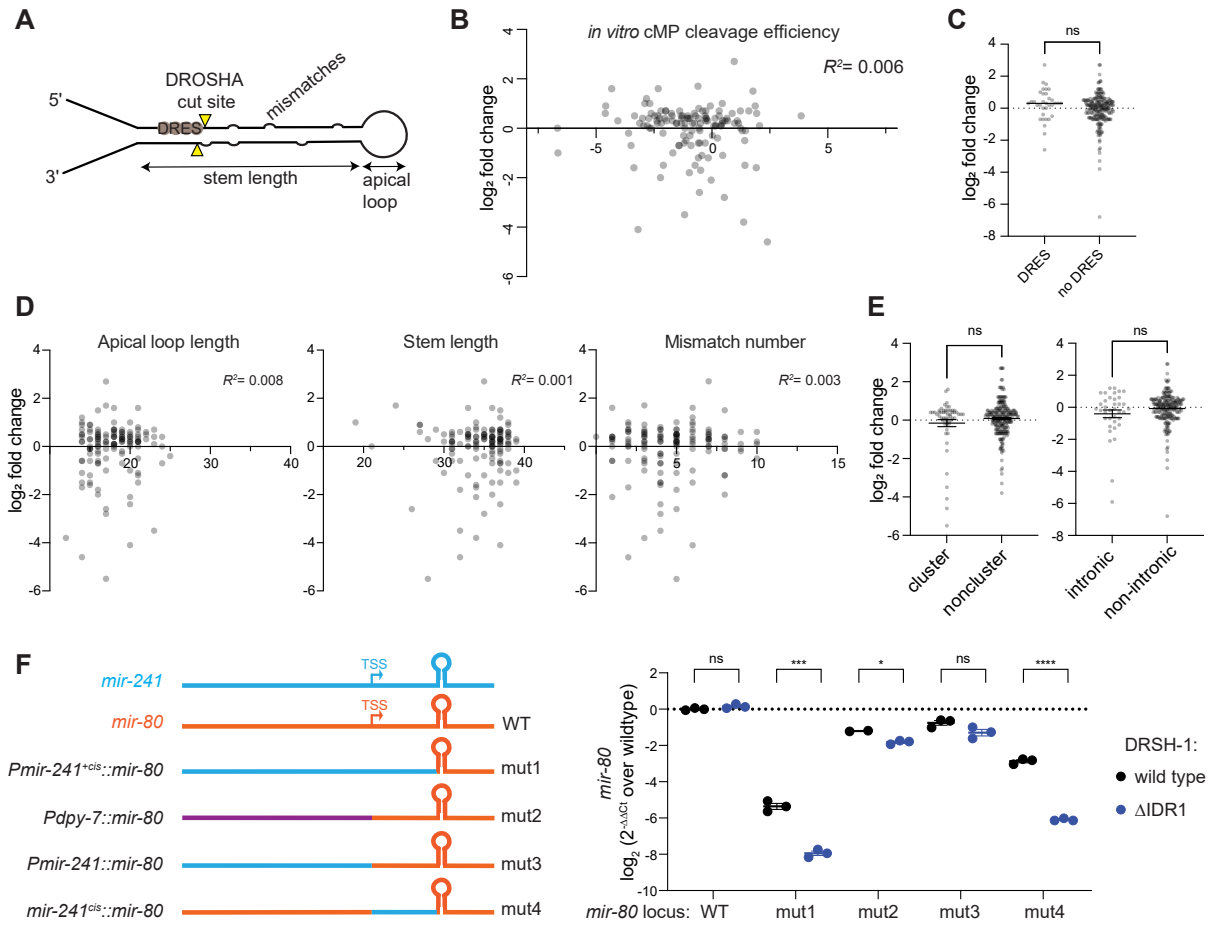

Figure 6. 5′ flanking sequence of miRNA confers IDR1-sensitivity. (A) Schematic diagram of local features of a pri-miRNA hairpin. (B) X-Y plot showing correlation between IDR1 sensitivity measured by miRNA $\log_2$ fold change (ΔIDR1/wild type L4) on the Y-axis and *in vitro C. elegans* Microprocessor cleavage efficiency from Nguyen, et al. 2023 on the X-axis. (C,E) IDR1 sensitivity between miRNA groups based on classifications: containing DROSHA dsRNA recognition sites (DRES) site or not in (C), clustering or standalone and intronic or exonic in (E). Two tailed unpaired Student's t-test, ns, not significant. (D) X-Y plots showing correlation between IDR1 sensitivity, and different predicted pri-miRNA secondary features, including apical loop length, stem length and mismatch number. (F) Left: Schematics showing genome edits made at the *mir-80* locus. Genomic structure of *pri-mir-241* is shown in blue, and orange shows the genomic structure of *pri-mir-80*. Hairpin structure depicts the pri-miRNA hairpin defined by the basal junctions. TSS denotes transcription start site. Right: *mir-80* Taqman qPCR comparing different mutants in DRSH-1 wild type or ΔIDR1 background. Two-tailed unpaired Student's t-test: (ns) not significant, (*) $P < 0.05$, (**) $P < 0.01$, (***) $P < 0.001$, (****) $P < 0.0001$.